11.2

EFFECTS OF NONSTATIONARY WAVE STRUCTURES ON ROTOR DEVELOPMENT AND EVOLUTION

Astrid Suarez* and David R. Stauffer
The Pennsylvania State University, University Park, PA

1. INTRODUCTION

Terrrain-induced gravity waves are rarely in steady state and have been shown to be effectively nonstationary, exhibiting a variety of frequencies in time and space, due to changes in background conditions and nonlinear phenomena. Three primary nonstationary behaviors have been identified in the literature: 1) downstream drifting of the wave pattern, 2) changes in horizontal wavelength, and 3) changes in the location and amplitude of local ridges and troughs (Nance and Durran 1997). Ralph et al. (1997) investigate 24 nonstationary wave events and show that mountain waves can exhibit 30% h^{-1} wavelength rate of changes associated with changes in background conditions. Idealized studies by Nance and Durran (1997, 1998) illustrate how wavelength transitions can enhance wave-wave interactions and temporarily affect the amplitude and structure of the waves.

Rotors (i.e., low level vortices generated by wave-induced pressure gradients) are highly coupled to the overlying wave structure. Changes in wave amplitude and location could impact their development and evolution. However little effort has been dedicated to the study of these nonstationary wave-rotor interactions or their subsequent impact on the stable boundary layer, where they can modulate the transport and dispersion.

In this study, the impact of nonstationary mountains waves due to mean flow variability and nonlinearity on rotor development and evolution is investigated for real cases over central Pennsylvania (PA). A combined observational and modeling approach is implemented 1) to provide evidence of complex waves and rotor structures generated by the moderate topography of central PA and 2) to investigate real cases characterized by nonlinear behavior and varying background conditions.

* *Corresponding author address:* Astrid Suarez, 623 Walker Building, Dept. of Meteorology, The Pennsylvania State University, University Park, PA 16802; email: ais5396@psu.edu

2. THE ROCK SPRINGS NETWORK AND OBSERVATIONS

A special observing network, deployed at Rock Springs, PA, is used to investigate gravity waves over the complex terrain of Central PA. The Rock Springs network is located within the Nittany Valley, 20 km southeast of the Allegheny Mountains and adjacent to Tussey Ridge (Fig 1a). The network consists of two SODARs, founded by the Army Research Office (ARO) Defense University Research Instrumentation Program (DURIP), as well as fast response two- and three-dimensional sonic anemometers and thermistor temperature sensors mounted on 2-, 10- and 50-m towers. These instruments are designed primarily for sampling downslope drainage winds and sub-mesoscale (scales < 2000 m) motions in the cold pools. The locations of the towers and SODARs are shown in Fig. 1b.

Two cases, exhibiting clear, calm conditions and complex wave and rotor structures, are investigated. The first case study, 24 August 2011 (AUG24 herein), is characterized by increasing pressure gradients due to an eastward propagating cyclone over the Great Lakes at 0000 UTC, south-southwesterly flow at ridge top, and gravity waves excited by Tussey Ridge. The second case study, 16 September 2011 (SEP16 herein), is characterized by decreasing pressure gradients as an anticyclone moves eastward over central PA by 1200 UTC, northwesterly flow at ridge top, and gravity waves generated by the Allegheny Mountains.

3. MODEL CONFIGURATION

Both cases are investigated using the Weather Research and Forecasting model (WRF) version 3.3.1 (Skamarock et al. 2008). The model is configured like that in Seaman et al. (2012). It includes four, one-way-nested domains with 12-, 4-, 1.33-, and 0.444-km horizontal grid spacing, respectively. For both cases, the model is initialized at 0000 UTC and integrated for 12 h using Global Forecast System (GFS) 0.5°x0.5°

initial and boundary conditions every 6 h. The model physics include the Noah land surface model coupled with the Moderate-resolution Imaging Spectroradiometer (MODIS) land use/land cover, the Mellor-Yamada-Janjic planetary boundary layer parameterization, the Rapid Radiative Transfer Model long-wave and Dudhia short-wave radiation schemes, and the Kain-Fritsch cumulus parameterization (12-km domain only).

4. NETWORK OBSERVATIONS

Time series of 2-m temperature at multiple sites throughout the Rock Springs network for AUG24 are presented in Fig 2a. This case is characterized by rapid cooling during the first three hours of the night, followed by a temperature increase of up to 7 K over a period of 10 min. The warming persists for the rest of the nighttime period, and it is briefly interrupted by periods of cooling between 0500-0530 UTC and 0600-0700 UTC. Sites located lower in the slope and thus deeper within the surface cold pool (e.g., site 12) experience larger temperature increases than those sites located higher in the slopes (e.g., site 6). For all sites, the onset of the warming is associated with wind speed increases from approximately 1 m s^{-1} prior to 0300 UTC to 5 m s^{-1} afterwards (not shown). SODAR observations (not shown) indicate that the onset of the warming is also associated with increasing low-level winds speeds, negative vertical motions of -2 m s^{-1}, and enhanced turbulent kinetic energy (TKE) below 180 m above ground level (AGL). The strong downward motions and TKE are associated with the downward branch of a lee-wave trough over the network. This case exhibits some characteristics of downslope windstorm events.

SEP16, on the other hand, is characterized by moderate cooling through the night and temperature fluctuations ranging from 1-3 K at multiple sites within the network (Fig 2b). Temperature fluctuations of ~3 K are noted from 0530-0900 UTC at all sites. As in AUG24, the largest temperature fluctuations are observed for sites embedded lower in the cold pool. SODAR 2027 observations for this case suggest the presence of a rotor circulation during the warming (Fig 3). This period exhibits weak wind speeds (< 2 m s^{-1}), and reversed, southeasterly flow below 100 AGL while the flow aloft remains primarily from the northwest (Fig 3). The onset of the reverse flow is associated with downward vertical motion and TKE exceeding 1.4 m^2 s^{-2}. This case exhibits characteristics of trapped waves and transient rotor structures.

5. MODEL RESULTS

5.1 AUG24 CASE STUDY

WRF forecasts at Site 9 for this case suggest that the model is able to capture some of the driving mechanisms for this case, but it has limited skill reproducing the correct amplitude and timing of the event. The forecasted temperature and wind behave similarly to that observed for this case study (not shown). However, the amplitude of the temperature and wind speed increases are underestimated at 3 K and 1 m s^{-1} (Fig 4a). It is important to note that larger temperature fluctuations (of up to 4 K) are noted just one grid point away (not shown).

A Hovmoller diagram of vertical velocity at 0.8 km mean sea level (MSL) for AUG24 on the 0.44-km domain reveals a change in wave structure through the night (Fig 5). Prior to 0500 UTC, the gravity waves are vertically propagating. This period is associated with weak shear and wind speed through the surface-based inversion near mountain top (not shown). Later periods are associated with the amplification of the waves (note the increasing vertical velocities) and the development of trapped modes within the valley. The first wave trough and crest exhibit the largest vertical velocity with wave energy rapidly decaying downstream (Fig 5). This period is associated with increased shear and wind speed through the inversion. Cross-sections of vertical velocity and potential temperature reveal the superposition of trapped and vertically propagating modes during this period (not shown).

The horizontal vorticity (associated with positive cross-mountain wind component defined to the left) and streamlines associated with the rotor circulation during the first and later part of the night are shown in Fig 6. During the first few hours of the night, a region of positive horizontal vorticity (out of page) becomes lofted by the upward branch of the wave at the boundary layer separation region adjacent to Tussey Ridge and it is advected downstream. No other coherent circulation is noted. During the later period, two distinct regions of positive horizontal vorticity appear to detach from the surface and become lofted by the upward branch of the wave. Note that the horizontal vorticity maxima are decoupled from one another.

WRF results for this case suggest that the different waves and rotor structures through the night have markedly different responses in the surface cold pool. During the first part of the night, the network is impacted by small wavelength, small amplitude waves with weak rotor circulation. This permits the development of a surface-based, strongly stratified layer near the surface. Changing background conditions result in increasing wavelengths and the amplification of the waves. The downward branch of the waves protrudes down the slope, bringing high momentum air down to the valley surface and temporarily displacing the cold pool. Periodic oscillations in wavelength and amplitude during the later period of the night, result in the displacement upstream of the lee wave trough (see oscillations in vertical velocity after 0600 UTC in Fig 5), permitting the brief reestablishment of the cold pool near the mountain.

5.2 SEP16 CASE STUDY

WRF does a reasonable job reproducing the observed temperature and wind speed trends for SEP16. For this case, the model forecasts temperature fluctuations of ~1 K during the first 4 h of the night (as observed in Fig 2b), followed by a temperature fluctuation of ~ 2 K from 0430-0700 UTC similar to that observed between 0530-0900 UTC (Fig 4b). WRF also produces wind speeds less than 1 m s^{-1} through the night, consistent with observations (Fig 4b). As for AUG24, WRF appears to be able to reproduce the driving dynamical processes for this case.

For SEP16, a Hovmoller diagram of vertical velocity at 1.5 km MSL shows transient wave structures (Fig 7). This case exhibits a ~7 km wavelength downstream of the Allegheny Mountains prior to 0300 UTC. This period is characterized by weak stability and strong shear near ridge top (not shown). The wave pattern appears to transition after this time as the stability increases and the wind speed and shear through the inversion weaken (not shown). A final wavelength of ~ 3 km is observed within the Nittany Valley by 1100 UTC. The reduction in wavelength is accompanied by the development of regions of constructive and destructive interference, where wave-wave interactions act to amplify or weaken the lee waves. The regions of constructive interference appear to move downstream, as the shorter wavelength pattern overtakes and interacts with the preexisting longer wavelengths. This behavior is consistent with that identified by Nance and Durran (1997) using idealized numerical simulations for changing background conditions from weakly to strongly stratified.

Regions of constructive interference and wave amplification during wavelength transitions impact the underlying rotor structure. A Hovmoller diagram of positive vertical velocity at 0.65 km MSL and reversed flow near the surface within the Nittany Valley is presented in Fig 8. Note that the strongest rotor circulation is not associated with the first wave crest (at 2 km). Instead, the strongest reversed flows are noted during periods of wavelength transitions and/or regions of wave amplification (possibly due to wave-wave interactions). Within the Nittany Valley, four periods of wavelength transition and enhanced reversed flows can be noted prior to 1200 UTC. The strongest reversed flow is associated with the first transitioning period occurring from 0200-0600 UTC, where the largest wavelength rate of change of ~ 15 % h^{-1} is observed. Note that the reversed flow regions propagate upstream along with the overlying wave pattern.

6. CONCLUSIONS

Observational evidence of complex wave structures and rotor circulations generated by the moderate terrain of Central Pennsylvania is presented. The waves and rotors can interact with the surface and modulate the evolution of the surface cold pool and the local stable boundary layer. WRF simulations for these cases have limited skill representing the correct timing and amplitude of the wave-cold pool interactions. However, the model appears to be able to resolve the driving mechanisms. The forecasted behavior of the waves and rotors generated by the moderate topography of Central PA appears to be consistent with those previously observed for large mountain ranges and simulated idealized conditions.

The waves and rotors generated for these cases exhibit nonstationary, transient behaviors that are highly coupled to changes in background conditions. Variations in the wave environment can lead to changes in the characteristic wavelength and complex wave-wave interactions leading to wave amplification. The intensity of the rotor reversal flow is associated with amplifying waves and periods of wavelength transitions where amplification due to constructive interference occurs. This relationship appears to hold for all wavelength rates of changes. Rotor propagation speed is similar to that of the transitioning wave pattern. Overall, nonlinear transient modes can act to enhance flow reversal and rotor intensity.

7. REFERENCES

Nance, L.B, and D.B. Durran, 1997: A modeling study of nonstationary trapped mountain lee waves. Part I: Mean-Flow Variability. *Journal of Atmospheric Sciences,* 54, 2275-2291.

Ralph, F.M., P.J. Neiman, T.L. Keller, D. Levinson, and L. Fedor, 1997: Observation, simulations and analysis of nonstationary trapped lee waves. *Journal of Atmospheric Sciences,* 54, 1308-1333.

Seaman, N.L., B.J. Gaudet, D. R. Stauffer, L. Mahrt, S.J. Richardson, J.R. Zielonka, and J.C. Wyngaard, 2012: Numerical prediction of the submesoscale flow in the nocturnal boundary layer over complex terrain. *Mon. Wea. Review*, 140, 956-997.

Skamarock, W.C., J.B. Klemp, J. Dudhia, D.O. Gill, D.M. Barker, W. Wang, and J.G. Powers, 2008: A description of the Advance Research WRF version 3. NCAR Tech Note NCAR/TN-468+STR.

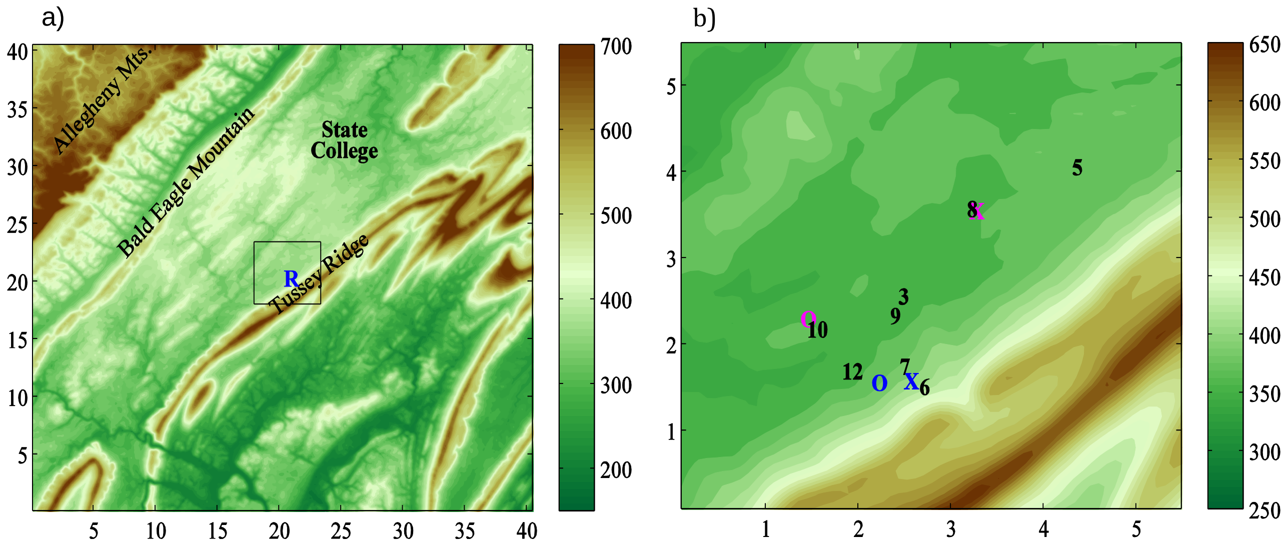

Figure 1. High-resolution (90-m) terrain elevation (m MSL, colored according to scale) for (a) a 40 km by 40 km region containing the Rock Springs network (R) and major topographical features and (b) a 5 km by 5 km region denoted by the black square in a) showing the distribution of instrumented towers and SODARs. X and O represent the locations of SODAR 2028 and 2027 respectively before (blue) and after (magenta) 29 September 2011, respectively.

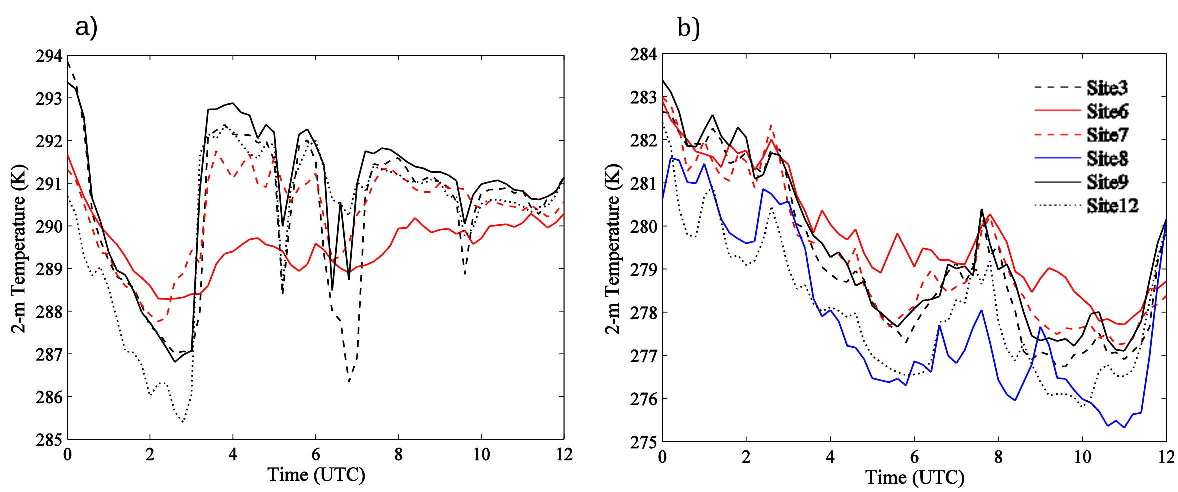

Figure 2. Time series of 2-m temperature at multiple sites within the Rock Springs network for (a) AUG24 and (b) SEP16.

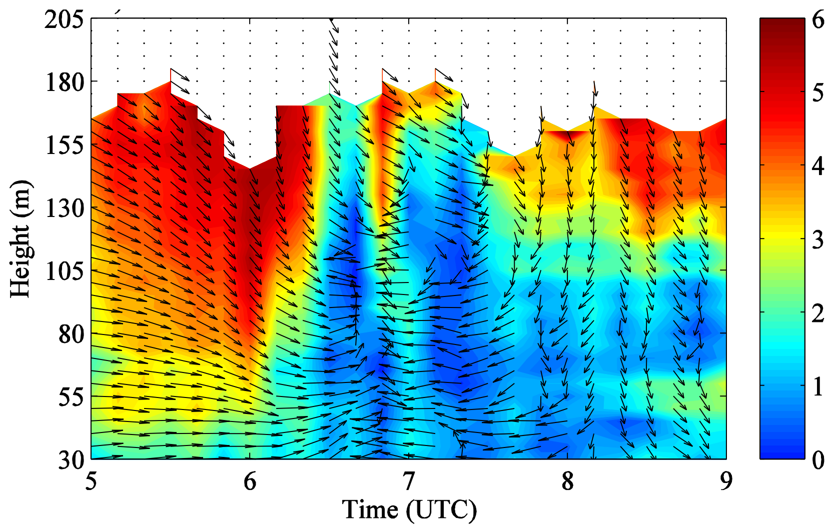

Figure 3. SODAR 2027 wind speed (m s^{-1}; colored according to scale) and horizontal wind vectors from 0500-0900 UTC for SEP16.

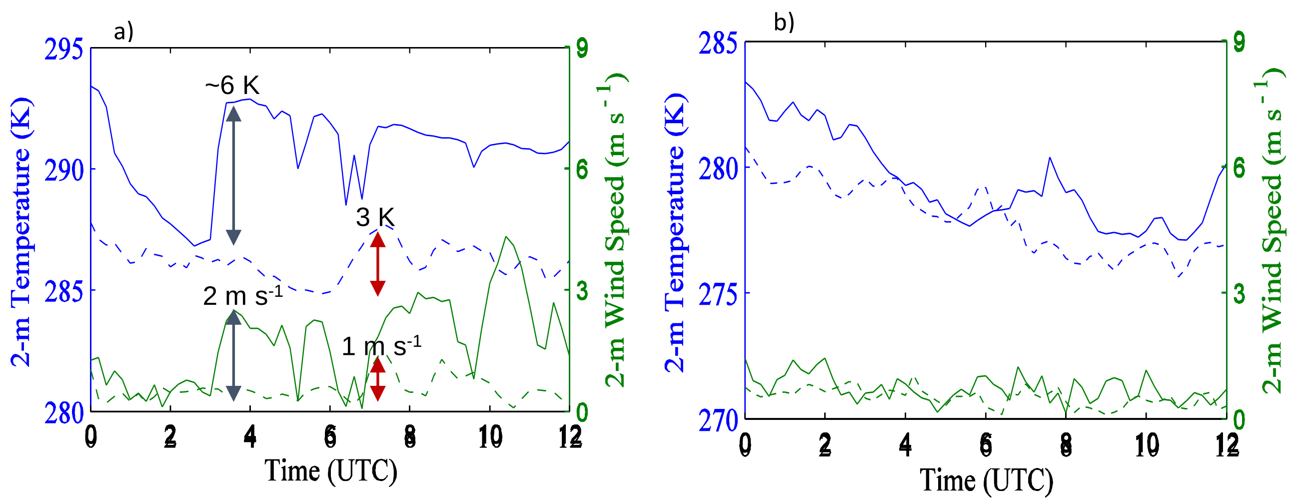

Figure 4. Observed (solid) and modeled (dashed) temperature and wind speeds over the 12-h forecast period for (a) AUG24 and (b) SEP16.

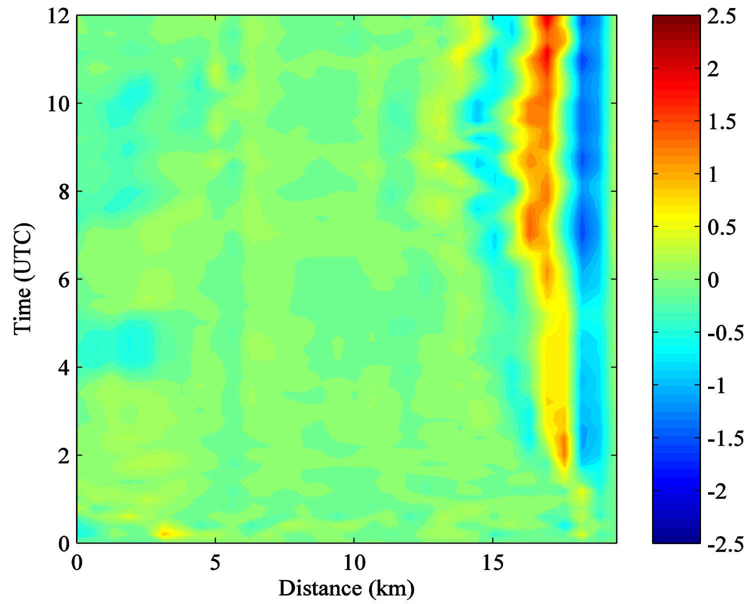

Figure 5. Hovmoller diagram of vertical velocity at 0.8 km MSL across the Nittany Valley, where Tussey Ridge is located near 20 km, for AUG24.

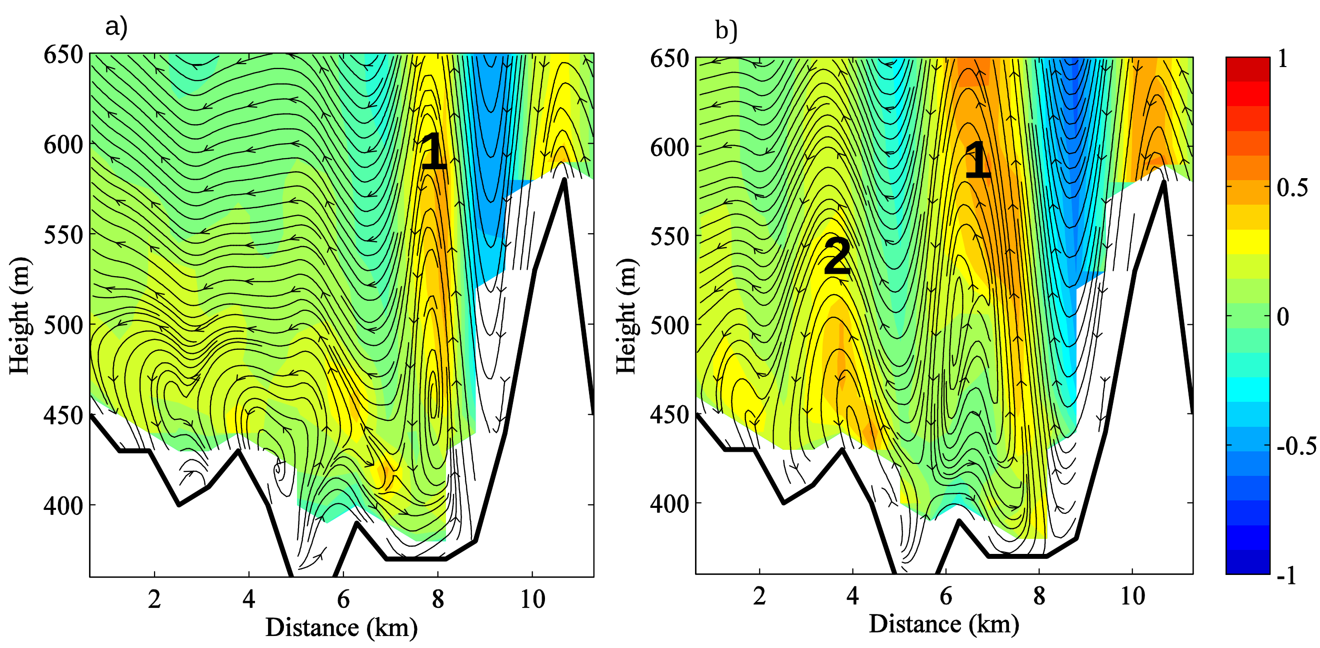

Figure 6. Cross-section of in-plane streamlines and horizontal vorticity (s^{-1}, shade according to scale) for AUG24 at (a) 0300 UTC and (b) 0900 UTC.

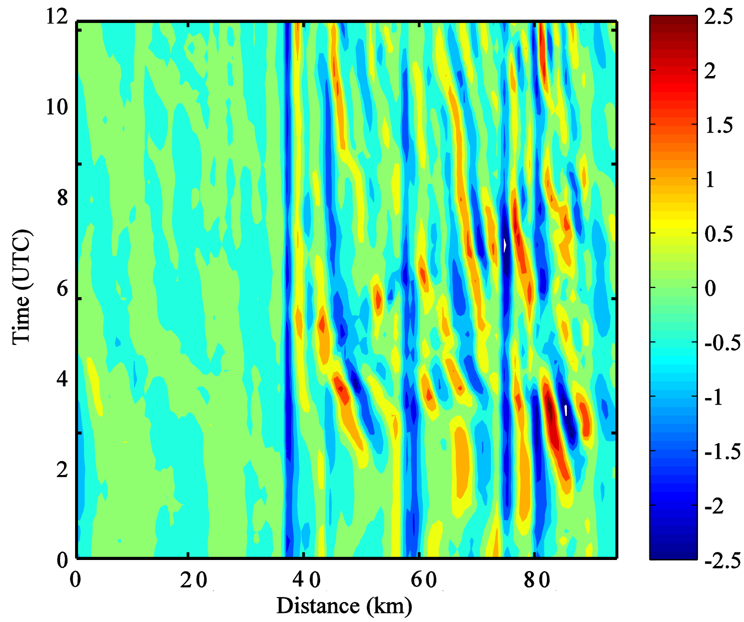

Figure 7. Hovmoller diagram of vertical velocity at 1.5 km MSL across the 0.44-km domain, where the Allegheny Mountains are near 38 km and Tussey Ridge is near 59 km, for SEP16.

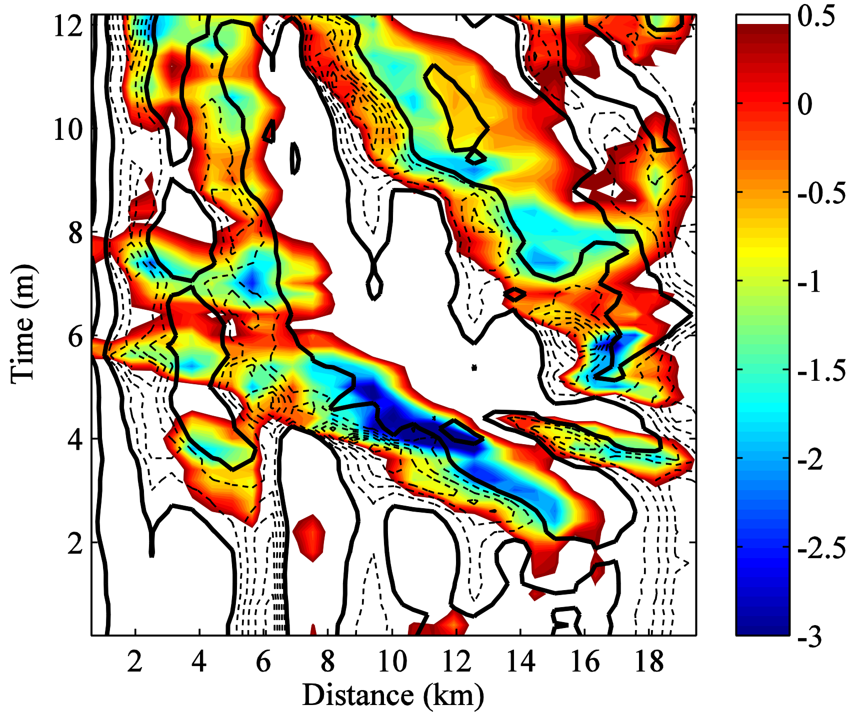

Figure 8. Hovmoller diagram of the cross-mountain wind component below 650 m AGL (m s^{-1}, shaded according to scale, positive to the right) and positive vertical velocities (dashed every 0.25 m s^{-1}; zero contour is in solid line) at 650 m showing reversed-flow regions propagating upstream (to the left).